TWENTY FIRST EUROPEAN ROTORCRAFT FORUM

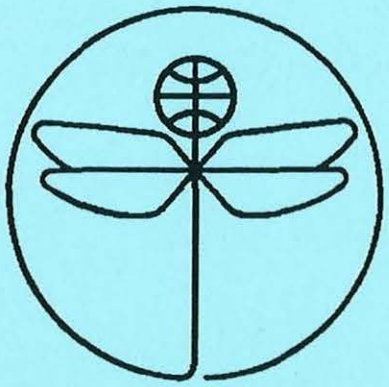

Paper No II.1

3D LAMINAR-TURBULENT BOUNDARY LAYER CALCULATIONS ON HELICOPTERS ROTORS IN FORWARD FLIGHT: APPLICATION TO DRAG PREDICTION

BY

Ph. Beaumier
ONERA
CHATILION, FRANCE
R. Houdeville
ONERA/CERT
TOULOUSE,FRANCE

August 30 - September 1, 1995
SAINT - PETERSBURG, RUSSIA

Paper nr.: II.1

3D Laminar-Turbulent Boundary Layer Calculations on Helicopter Rotors in Forward Flight: Application to Drag Prediction.

P. Beaumier; R. Houdeville

TWENTY FIRST EUROPEAN ROTORCRAFT FORUM
August 30 - September 1, 1995 Saint-Petersburg, Russia

3D LAMINAR-TURBULENT BOUNDARY LAYER CALCULATIONS ON HELICOPTER ROTORS IN FORWARD FLIGHT: APPLICATION TO DRAG PREDICTION [1]

Philippe BEAUMIER
ONERA
29 Avenue de la Division Leclerc
CHATILLON - FRANCE

Robert HOUDEVILLE
ONERA/CERT
2 Avenue Edouard Belin
TOULOUSE - FRANCE

Abstract

The calculations presented in this paper are a first step towards the prediction of the total power consumed by an helicopter rotor in forward flight. The 3D unsteady full potential code *FP3D* is coupled with a boundary layer code which solves the 3D unsteady global equations and includes the prediction of transition. Results obtained for a particular rotor at two advance ratios (0.3 and 0.45) are presented. The prediction of the transition location is compared to experimental results based on hot film measurements. The calculated power friction consumed by the rotor is given and compared to the experimental total power.

1 Introduction

Despite the development of more and more sophisticated methods, drag prediction on helicopter blades is still a challenging problem for aerodynamicists. Unsteady wave drag, induced drag and friction drag are the three largest components of the total drag and consequently of the total power consumed by the rotor.

The estimation of rotor performance by helicopter manufacturers is most of the time provided by very simple inviscid aerodynamic models (the majority is based on lifting-line theory) with the use of 2D airfoil tables to account for viscous effects on C_l, C_m and C_d coefficients. If these models provided generally good agreement with experiments for conventional rotors (rectangular blades), it seems that their limits are reached with the generation of blades that presently equip helicopters. This is due to important 3D effects that may occur and modify the aeroelastic behaviour of the rotor and consequently the power consumed.

In parallel to these simple methods, more sophisticated (and time consuming) CFD techniques have been developed in order to be able to calculate the complex 3D aerodynamical phenomena occuring on such blades. ONERA has made special efforts for several years to calculate the power consumed by a rotor with the use of such methods.

In this paper, CFD methods are used with the goal of calculating the viscous friction power consumed by helicopter rotors in forward flight configurations. In a first part, the computational tools used in this study are presented. They consist in a weak coupling between a well known 3D full potential code for inviscid calculations with a 3D integral boundary layer code for the computation of viscous effects around the blades. Emphasis is put on the boundary layer code with a particular care on laminar-turbulent transition prediction and modelling. In a second part, that method is applied and validated on two configurations of a lifting rotor in moderate and high speed configurations. Boundary layer calculations are compared with experimental results for the transition locations and an estimate of the friction power consumed by the blades is provided and compared to total experimental power.

2 Calculation methods

2.1 Boundary layer integral method

The boundary layer equations are written in a general curvilinear body fitted coordinate system. Although the present application case to a helicopter blade uses only an orthogonal axis system, the

[1] work has been financially supported by DRET

method has been developed and will be presented for the general case. The surface over which the boundary layer spreads is defined using the x^i-coordinates of a point P in it (Fig. 1):

$$x^i\left(X^1, X^2\right) \qquad i = 1, 2, 3 \tag{1}$$

(X^1, X^2) are the generalized coordinates of the surface. $\overrightarrow{e_1}$ and $\overrightarrow{e_2}$ generate the local reference frame in the surface and $\overrightarrow{e_3}$ is normal to $\overrightarrow{e_1}$ and $\overrightarrow{e_2}$ which might not be orthogonal. We have (see for example Hirschel-Kordulla [15]):

$$\overrightarrow{e_1} = \frac{\partial x^i}{\partial X^1}\overrightarrow{e_i} \qquad \overrightarrow{e_2} = \frac{\partial x^i}{\partial X^2}\overrightarrow{e_i} \qquad i = 1, 2, 3 \tag{2}$$

The metric tensor is given by $g_{ij} = \overrightarrow{e_i}.\overrightarrow{e_j}$. According to the thin layer hypotheses, g_{ij} are assumed constant in the boundary layer thickness and $g_{33} = 1$. In the present paper, the notations of figure 2 will be considered:

$$h_1^2 = g_{11} \;\; ; \;\; h_2^2 = g_{22} \;\; ; \;\; h_1 h_2 \cos\lambda = g_{12} = g_{21} = g \;\; ; \;\; h_1 h_2 \sin\lambda = q \tag{3}$$

2.1.1 Integral boundary layer equations

The global equations are obtained by integrating the local equations from the surface to the outer edge of the boundary layer. For a three-dimensional, unsteady and compressible flow in a rotating reference frame, the continuity and momentum global equations read [19, 11, 10]:

$$\frac{1}{q\rho_e u_e}\frac{\partial}{\partial X}\left[\rho_e u_e \frac{q}{h_1}\left(\delta\frac{U_e}{u_e} - \Delta_1\right)\right] + \frac{1}{q\rho_e u_e}\frac{\partial}{\partial Z}\left[\rho_e u_e \frac{q}{h_2}\left(\delta\frac{W_e}{u_e} - \Delta_2\right)\right] =$$

$$\frac{U_e}{u_e}\frac{1}{h_1}\frac{\partial\delta}{\partial X} + \frac{W_e}{u_e}\frac{1}{h_2}\frac{\partial\delta}{\partial Z} - \frac{v_e}{u_e} + \frac{1}{\rho_e u_e}\frac{\partial}{\partial t}\rho_e\delta_\rho - \frac{\delta}{\rho_e u_e}\frac{\partial\rho_e}{\partial t} \tag{4a}$$

$$\frac{1}{h_1}\frac{\partial\Theta_{11}}{\partial X} + \Theta_{11}\left[\frac{1}{q\rho_e u_e^2}\frac{\partial}{\partial X}\left(\frac{q}{h_1}\rho_e u_e^2\right) + k_1\right] + \frac{1}{h_2}\frac{\partial\Theta_{12}}{\partial Z} + \Theta_{12}\left[\frac{1}{q\rho_e u_e^2}\frac{\partial}{\partial Z}\left(\frac{q}{h_2}\rho_e u_e^2\right) + k_3\right]$$

$$+\Delta_1\left(\frac{1}{u_e h_1}\frac{\partial U_e}{\partial X} + k_1\frac{U_e}{u_e} - \frac{2\omega_3}{u_e}\frac{1}{\tan\lambda}\right) + \Delta_2\left(\frac{1}{u_e h_2}\frac{\partial U_e}{\partial Z} + k_2\frac{W_e}{u_e} + k_3\frac{U_e}{u_e} - \frac{2\omega_3}{u_e}\frac{1}{\sin\lambda}\right)$$

$$+k_2\Theta_{22} + \frac{1}{\rho_e u_e^2}\frac{\partial}{\partial t}\left(\rho_e u_e\Delta_1\right) - \frac{U_e}{\rho_e u_e^2}\frac{\partial}{\partial t}\left(\rho_e\delta_\rho\right) + \frac{\Gamma_{eX}}{u_e^2}\delta_\rho = \frac{C_{fX}}{2} \tag{4b}$$

$$\frac{1}{h_1}\frac{\partial\Theta_{21}}{\partial X} + \Theta_{21}\left[\frac{1}{q\rho_e u_e^2}\frac{\partial}{\partial X}\left(\frac{q}{h_1}\rho_e u_e^2\right) + l_3\right] + \frac{1}{h_2}\frac{\partial\Theta_{22}}{\partial Z} + \Theta_{22}\left[\frac{1}{q\rho_e u_e^2}\frac{\partial}{\partial Z}\left(\frac{q}{h_2}\rho_e u_e^2\right) + l_2\right]$$

$$+\Delta_1\left(\frac{1}{u_e h_1}\frac{\partial U_e}{\partial X} + l_1\frac{U_e}{u_e} + l_3\frac{W_e}{u_e} + \frac{2\omega_3}{u_e}\frac{1}{\sin\lambda}\right) + \Delta_2\left(\frac{1}{u_e h_2}\frac{\partial W_e}{\partial Z} + l_2\frac{W_e}{u_e} + \frac{2\omega_3}{u_e}\frac{1}{\tan\lambda}\right)$$

$$+l_1\Theta_{11} + \frac{1}{\rho_e u_e^2}\frac{\partial}{\partial t}\left(\rho_e u_e\Delta_2\right) - \frac{W_e}{\rho_e u_e^2}\frac{\partial}{\partial t}\left(\rho_e\delta_\rho\right) + \frac{\Gamma_{eZ}}{u_e^2}\delta_\rho = \frac{C_{fZ}}{2} \tag{4c}$$

In these equations, U_e and W_e are the components, expressed in physical units, of the external velocity in the surface reference frame and u_e is the magnitude of the outer velocity, equal to the inviscid velocity at the skin of the rotor blade: C_{fX} and C_{fZ} are the values of the skin friction coefficient in the directions $X \equiv X^1$ and $Z \equiv X^2$, respectively. The definitions of the integral thicknesses in that frame are the following:

$$\Delta_1 = \int_0^\delta\left(\frac{U_e}{u_e} - \frac{\rho U}{\rho_e u_e}\right)dy \;;\; \Delta_2 = \int_0^\delta\left(\frac{W_e}{u_e} - \frac{\rho W}{\rho_e u_e}\right)dy \;;\; \Theta_{11} = \int_0^\delta\frac{\rho U}{\rho_e u_e^2}\left(U_e - U\right)dy \tag{5a}$$

$$\Theta_{12} = \int_0^\delta\frac{\rho W}{\rho_e u_e^2}\left(U_e - U\right)dy \;;\; \Theta_{21} = \int_0^\delta\frac{\rho U}{\rho_e u_e^2}\left(W_e - W\right)dy \;;\; \Theta_{22} = \int_0^\delta\frac{\rho W}{\rho_e u_e^2}\left(W_e - W\right)dy \tag{5b}$$

$$\delta_\rho = \int_0^\delta \left(1 - \frac{\rho}{\rho_e}\right) dy \; ; \; u_e^2 = U_e^2 + W_e^2 + \frac{2g}{h_1 h_2} U_e W_e \tag{5c}$$

In the equations, k_i and l_i are functions of the metric coefficients g_{ij} [9]. The Coriolis acceleration is taken into account through ω_3, the component of the rotation vector normal to the surface. Γ_{eX} and Γ_{eZ} are the centripetal acceleration components, the influence of which vanishes in incompressible flow since $\delta_\rho = 0$.

2.1.2 Principle of the integration

The large number of unknowns appearing in the integral equations 4a-4c needs to consider closure relationships. The integral thicknesses 6a 6b expressed in the streamline coordinate system are more suitable than the expressions 5a 5b which depend on the choice of the body fitted coordinate system. In the following definitions, u is along the external velocity direction and w is in the crossflow direction:

$$\delta_1 = \int_0^\delta \left(1 - \frac{\rho u}{\rho_e u_e}\right) dy \quad ; \quad \delta_2 = \int_0^\delta - \left(\frac{\rho w}{\rho_e u_e}\right) dy \quad ; \quad \theta_{11} = \int_0^\delta \frac{\rho u}{\rho_e u_e} \left(1 - \frac{u}{u_e}\right) dy \tag{6a}$$

$$\theta_{12} = \int_0^\delta \frac{\rho w}{\rho_e u_e} \left(1 - \frac{u}{u_e}\right) dy \quad ; \quad \theta_{21} = \int_0^\delta - \left(\frac{\rho w u}{\rho_e u_e^2}\right) dy \quad ; \quad \theta_{22} = \int_0^\delta - \left(\frac{\rho w^2}{\rho_e u_e^2}\right) dy \tag{6b}$$

By simply considering a change of reference frame, Θ_{ij}, Δ_i and C_{fX}, C_{fZ} are explicit functions of θ_{ij}, δ_i and C_{fx}, C_{fz}, respectively, including λ and α (Fig. 2). Substituting these relations into the global equations, a new set of 3 equations for the 10 unknowns $\delta_1, \delta_2, \theta_{11}, \theta_{12}, \theta_{21}, \theta_{22}, C_{fX}, C_{fZ}, \delta$ and δ_ρ is obtained. To integrate it, θ_{11}, $H = \delta_1/\theta_{11}$ and θ_{21} are chosen as the main unknowns. Moreover, in order to get a set of equations to integrate as implicit as possible, 3 new functions are introduced to express δ_2, θ_{22}, $\theta_{12} = \theta_{21} - \delta_2$ and $\delta - \delta_1$, as well as their time-derivatives, as functions of the main unknowns. These functions are:

$$C_2 = \frac{\delta_2}{\theta_{21}} \quad ; \quad C_{22} = \frac{\theta_{11}\theta_{22}}{\theta_{21}^2} \quad ; \quad H^* = \frac{\delta - \delta_1}{\theta_{11}} \tag{7}$$

They are explicit functions of M_e, the local Mach number, and $H = \delta_1/\theta_{11}$ because of the chosen relationships.

The integration from point (X, Z, t) to $(X + \Delta X, Z, t)$ is done by inverting a $3X3$ matrix for the 3 main unknowns. The matrix coefficients are taken at point (X, t). A subgrid is used in the X direction. The Z-derivatives which apply to Δ_2, Θ_{12} and Θ_{22} (equations 4a 4b and 4c) are left in the right hand side of the equations and are explicitly discretized to the first order in the upwind direction. The details of the method can be found in reference [16].

2.1.3 Closure relationships

The establishment of closure relationships is based on the integration of local boundary layer equations in which a local similarity hypothesis is made for the longitudinal and transversal velocity components: $u/u_e = f'(y/\delta)$, $w/w_e = g'(y/\delta)$. For compressible flow, the parameters are the Reynolds number, the longitudinal and transversal pressure gradients and the Mach number. The efficiency of any integral method is closely dependent on the skillfulness of the designer to choose the correct basic parameters and find the analytic forms of the relationships. In this way, the two pressures gradient parameters must not explicitly appear in the closures relationships. For a complete discussion of these problems, one can refer to references [9, 10].

2.1.4 Transition to turbulence

The calculation of the laminar-turbulent transition region involves two problems: *i)* the determination of the onset of the transition region, *ii)* the calculation of this region itself. In the present method, the boundary layer is assumed fully turbulent just after the onset of transition; the shape parameter is set equal to $1.4 + 0.4M_e^2$ and the continuity of θ_{11} and θ_{21} is assumed. As far as the onset of transition is concerned, various mechanisms are considered. They are:

a) longitudinal instability mode: this mode of instability corresponds to the amplification of Tollmien-Schlichting waves as in 2D boundary layers. An extension of the Granville criterion [14] proposed by Arnal *et al.* [5, 1] in order to take into account the influence of external turbulence is used. This criterion also includes the pressure gradient effects.

b) transversal instability mode: for 3D boundary layers, the transition can occur in regions where the streamwise velocity profile is stable. In this case it is the crossflow velocity profile which can be unstable. From experimental data, Arnal *et al.* [2, 3, 4] have extended the Beasley criterion [6] to take into account the effects of streamwise pressure gradients.

c) laminar separation: the boundary layer is imposed turbulent just at the laminar separation point.

d) displacement of the transition line: as the flow is unsteady, the transition line oscillates but this displacement is not symmetric as shown by Desopper [13]. The downstream displacement corresponds to a sweeping of the turbulence by the flow. It occurs at a limited speed, in the range 0.5 to 0.7 of the external velocity. On the other hand, the velocity of the upstream displacement of the transition line is not limited because it is due to the growing of instabilities coming from upstream.

The unsteady displacement of transition line complicates the use of the transition criteria because the thicknesses and the shape factor of the laminar boundary layer must be known, instead of the actual boundary layer parameters. To solve this problem, a fictitious laminar boundary layer is calculated and stored downstream the transition point, up to the separation point.

2.1.5 Boundary layer initialization

At each time step, the boundary layer is initialized near the attachment line of the rotor blade. For this, similarity solutions for an infinite swept wing give θ_{11} and θ_{21} knowing the local velocity gradient in the direction perpendicular to the leading edge. At the initial time, a quasi-steady calculation is done by neglecting the time derivatives.

2.2 Coupling with a 3D unsteady potential method

In order to run the boundary layer code presented before, it is necessary to know the 3D components of the velocity field outside the boundary layer. For all the calculations presented in this paper, this is done by the 3D unsteady full potential code *FP3D* [7].

For uncoupled calculations, *FP3D* code is run for one rotor revolution. It gives the velocity components (Ue,Ve,We) and the density ρ_e at each mesh point on the blade surface and for each desired blade azimuth. A typical time step for those outputs has been chosen equal to 1°. Then, boundary layer calculations are performed for one rotor revolution, with 1° time step, too. The drawback of this simple method is that it does not account for the effect of boundary layer on the inviscid calculations performed by *FP3D*. A more precise method can be applied: it consists in performing a weak coupling at each time step between the potential code *FP3D* and the boundary layer code. This method has been successfully developed at ONERA [8] and is briefly described below.

The effect of boundary layer on potential calculations is modelled by the so called "transpiration condition": a non zero velocity normal to the airfoil accounts for the thickening of the airfoil due to the boundary layer. An equivalent transpiration angle ϵ is calculated using equation:

$$\epsilon = \frac{V^*}{u_e} = \frac{1}{\rho_e u_e}\frac{\partial \rho_e \delta_\rho}{\partial t} + \frac{1}{\rho_e u_e q}\frac{\partial}{\partial X}\left(\frac{\rho_e u_e q}{h_1}\Delta_1\right) + \frac{1}{\rho_e u_e q}\frac{\partial}{\partial Z}\left(\frac{\rho_e u_e q}{h_2}\Delta_2\right) \qquad (8)$$

The application of this equation may raise some problems when the boundary layer displacement thicknesses are not calculated. This happens in particular: a- near trailing edge because the present method cannot calculate separated flows, b- in limited separated regions due to shock wave recompressions, c- when massive separation occurs in the retreating side of the rotor disk. An extrapolation of transpiration angles is performed in case a-: it consists in continuously reducing the X derivative of the angle ϵ from the last calculated point to the trailing edge (Ref. [17]). In case b-, a simple linear interpolation is performed. For case c-, a constant angle ϵ is used all along the airfoil: this treatment

has no physical basis but is done in order to avoid numerical divergence. The scheme of this weak coupling is summarized in Fig. 3. Practically, the mean time step used in *FP3D* code is 0.1° and the coupling with the boundary layer is performed every 10 time steps. Between two boundary layer calculations, the transpiration angles ϵ are kept constant. This simple procedure is just an efficient way to reduce the computational effort and does not change the results of the calculations (in terms of pressure distribution or even friction power).

3 Applications

3.1 Test cases

The present computational method is applied to some realistic configurations taken from the 11^{th} helicopter campaign performed in ONERA/S1MA wind tunnel in 1991 [18, 12]. Among the rotors tested during this campaign, the so called "7A" rotor has 4 blades with a diameter equal to 4.2 meters. The blades are rectangular with a mean chord of 0.14 m and an aspect ratio equal to 15. Their cross-section is an OA213 airfoil up to section r/R = 0.7 and an OA209 airfoil from r/R = 0.9 to the tip, with a linear geometric interpolation in between.

Two different calculations are presented here, both simulating a rotor in forward flight with a tip rotating Mach number $M_{\Omega R}$ equal to 0.646 and a total drag coefficient $(C_dS)/S\sigma$ equal to 0.1. For the first case, the advance ratio is moderate, (μ= 0.3) and the thrust coefficient C_t/σ equals 0.0625. For the second case, μ is higher, equal to 0.45 and C_t/σ= 0.075.

The "7A" blades were instrumented with 116 pressure transducers distributed over 5 sections located at r/R = 0.5, 0.7, 0.825, 0.915 and 0.975; thus, it has been possible to compare results given by *FP3D* code with experimental pressure distributions. Furthermore, some measurements were done using hot films located mainly on the section r/R = 0.9: the interpretation of these measurements has led to very interesting conclusions concerning the location of transition from laminar to turbulent [20]. These results will be compared to those obtained with the present boundary layer method.

3.2 Results

Pressure distribution. An example of calculated and experimental pressure distributions is provided in Fig. 4 at ψ= 90°. Generally speaking, calculations are in a rather good agreement with experiment for all sections.

The strong shock waves are clearly visible, particularly at r/R = 0.975. *FP3D* calculations without boundary layer corrections tend to overestimate the extent of supersonic flows and consequently to predict shock waves at a location further downstream than in the experiment. This is a general feature from inviscid methods. For the present case, coupled and uncoupled calculations provide very close results.

However, the shock wave positions predicted by the coupling procedure are slightly in a better agreement with experiment than without any coupling: this effect is typically what could be expected from viscous corrections but appears to be very small here. Near the trailing edge, some very small differences between coupled and uncoupled calculations occur; they are due to the thickening of the boundary layer.

Skin friction lines. The calculated skin friction lines are plotted in Fig. 5 on the upper surface for the blades located at 4 different azimuths: 0°(rear blade), 90° (advancing blade), 180°and 270° (retreating blade). In a small area near the trailing edge of the blades, skin friction lines suddenly stop. This could correspond to either a physical separation or a numerical instability (which is more likely the case, except at ψ= 270° where physical separations may occur). On the advancing side (ψ= 90°), the dotted line in Fig. 5 indicates that the calculation stops because of strong recompressions due to shock waves. A special treatment allows us to calculate the boundary layer even after these recompressions. However, a large portion of the surface of the blades is calculated (80 to 100%

depending on the azimuth), demonstrating the robustness of the method. Finally, the 3D nature of the flow is very clear near the blade tip, particularly at $\psi = 180°$.

Transition between Laminar and Turbulent boundary layers. Fig. 8 presents a visualization of the calculated state of the boundary layer. For the case with a moderate advance ratio ($\mu = 0.3$), a small laminar area can be seen near the leading edge of the upper surface on the advancing side ($\psi = 90°$). After this area, the boundary layer becomes turbulent. On the lower surface, the boundary layer is almost always turbulent.

For the other case (high advance ratio: $\mu = 0.45$), the extent of the laminar area on the upper surface is more increased: this is a consequence of the strong acceleration of the flow due to very important shock waves mentioned above (see Fig. 4). A strange "gap" appears in this laminar area near r/R = 0.9: in this case, the longitudinal criterion predicts a transition at a location far upstream of the shock wave.

The nature of the boundary layer is totally different in the retreating side (for $\mu = 0.3$ for example): this time, the boundary layer is turbulent on the upper surface and mostly laminar on the lower surface because of the very high incidences which create large accelerations on the lower surface and large decelerations on the upper surface. But the most interesting feature to point out is the time evolution of the transition between laminar and turbulent boundary layer (Fig. 6-7-9). For this, the section located at r/R= 0.9 has been chosen because it is equipped with hot films. It should be mentioned here that the experimental position of transition is not measured directly by hot films. They only provide information about the nature of boundary layer (laminar or turbulent) at their own location. The transition location is known with an uncertainty more or less important depending on the azimuth angle, as explained in Ref. [20].

For the case with $\mu = 0.3$ on the upper surface (Fig. 6), the correlation between calculations and hot film measurements is reasonably good, showing that the extent of the laminar boundary layer is larger between 30 and 240° than between 240 and 30°. Calculations tend to predict a transition closer to the leading edge than experiment (x/c = 25% instead of x/c = 35% at $\psi = 90°$). For the case with $\mu = 0.45$ on the upper surface (Fig. 7), both calculations and experiment predict an increase of the laminar zone on the advancing side and almost no laminarity on the retreating side. It is difficult to say whether the calculation on the advancing side is close to experiment or not because of the large experimental uncertainty.

On the lower surface for $\mu = 0.3$ (Fig. 9), the correlation between calculations and hot film measurements is reasonably good: the quick evolution of the transition between 180 and 200° is well calculated. On the retreating side, the extent of the laminar zone seems in good agreement with experiment, too.

Friction power. The final goal of present computational method is the prediction of the total power consumed by an helicopter rotor in forward flight. One of the terms involved in power consumption comes from viscous friction drag. A direct integration of wall shear stress on a blade section provides the 3 components of elementary viscous forces applied on each blade section. As an example, longitudinal (Fx) and transversal (Fy) forces are plotted as a function of spanwise position in Fig. 10.

Drag force Fx increases from 30° to 90° azimuth and then decreases from 90° to 150°, which is a consequence of the blade velocity variation on the advancing side. Friction drag on sections located more inboard (index 1 corresponding to r/R = 0.5) is greater than friction drag on sections located near the blade tip (index 18 for r/R = 1), which may be surprising because blade tip sections have a larger velocity: this is explained by the mesh refinement near the tip so that the force on the sections at the tip corresponds to smaller surfaces than the force on inboard sections.

Side force Fy is almost symmetrical around azimuth 90°and is naturally more important for $\psi = 150°$ and 30° than $\psi = 90°$ because in these areas the free-stream velocity has an important transverse component. The lift force Fz (not plotted here) is negligible. By multiplying these 3 components by the blade section velocities, one can easily obtain the corresponding friction power consumption. Friction power is approximately a sinusoidal function of azimuth angle (Fig. 11 for $\mu = 0.3$) with a maximum near $\psi = 90°$ and a minimum near $\psi = 270°$, on both upper and lower surfaces.

μ	upper surface	lower surface	Total friction power (4 blades)	Experiment Total power	Tot. friction power / tot. expe. power
0.3	1.78 kW	1.69 kW	13.88 kW	48.67 kW	29%
0.45	2.00 kW	2.14 kW	16.56 kW	125.02 kW	13%

Table 1: Comparison of calculated friction power with total experimental power

It is interesting to compare laminar+turbulent boundary layer calculations with fully turbulent calculations: the last model tends to provide larger values for friction power on the advancing side near $\psi = 90°$ (upper surface) and on the retreating side around $\psi = 270°$ (lower surface) than the model in which transition is calculated: this is very coherent with the laminar areas pointed out above. For the highest advance ratio ($\mu = 0.45$: Fig. 12), the effect of a fully turbulent calculation compared to a laminar+turbulent calculation is increased on the upper surface on the advancing side, as a consequence of the increase of the extend of the laminar zone with advance ratio, as pointed out before.

A time average provides the friction power mean value consumed by the rotor during one revolution. These values are summarized in Tab. 1. In fact, friction power slightly increases from $\mu = 0.3$ to $\mu = 0.45$.

It is not possible to directly compare these results with experiment since it only provides the total power (including friction, wave, induced ... drag). However, Tab. 1 shows that friction power represents 29% of the total experimental power at $\mu = 0.3$ and only 13% at $\mu = 0.45$: this trend seems coherent, since at $\mu = 0.45$ most of the power is probably due to shock wave power. The effect of laminarity on total friction power is small, although not negligible (Fig. 13): taking into account a laminar+turbulent model instead of a pure turbulent model decreases friction power by 2% of experimental total power, for the two cases studied here.

4 Conclusion

A 3D CFD method based on the weak coupling between a full potential code and a laminar-turbulent boundary layer code has been developed and validated on a helicopter rotor in moderate and high speed configurations. The boundary layer code robustness has been demonstrated in some configurations where strong shock waves are present; physical separations cannot be calculated but do not alter the code robustness. The predicted laminar-turbulent transition has been successfully compared with indicators provided by hot films: the time evolution of the transition is in reasonably good agreement with experiment. As an application, the viscous friction drag has been calculated for one rotor revolution and compared with experimental total power: friction drag represents 29% of total power for a moderate advance ratio (μ= 0.3) and only 13% for a high advance ratio (μ= 0.45).

At this point of the study, it is clear that only one part of the power consumed by the rotor has been calculated. A method based on momentum conservation equations is under development at ONERA in order to be able to evaluate the unsteady wave and induced drag components.

References

[1] D. Arnal : *Description and prediction of transition in two-dimensional, incompressible flow.* AGARD Report N°709 Special Course on Stability and Transition of Laminar Flow 1984

[2] D. Arnal : *Three-dimensional boundary layers : Laminar-turbulent transition.* Lecture Series on Computation of Thee-dimensional boundary layers including separation. V.K.I. 1986

[3] **D. Arnal, E. Coustols :** *Application de critères bi- et tridimensionnels au calcul de la transition et de la couche limite d'ailes en flèche* Symposium AGARD "Improvement of aerodynamic performance through boundary layer control and high lift systems" Bruxelles mai 1984

[4] **D. Arnal, M. Habiballah, E. Coustols :** *Théorie de l'instabilité laminaire et critères de transition en écoulement bi et tridimensionnel.* La Recherche Aérospatiale 1984-2 (french and english edition)

[5] **D. Arnal, M. Habiballah, V. Delcourt :** *Synthèse sur les méthodes de calcul de la transition développées au DERAT.* Note Technique DERAT 11/5018 DY 1980

[6] **J.A. Beasley :** *Calculation of the laminar boundary layer and the prediction of the transition on a sheared wing.* ARC R&M 3787 1973

[7] **P. Beaumier, M. Costes, R. Gaveriaux :** *Comparison between FP3D Full Potential calculations and S1 Modane Wind Tunnel test results on advanced fully instrumented rotors* , 19th European Rotorcraft Forum, Cernobbio, Como (Italy), September 14-16, 1993

[8] **M. Costes, M. Rahaingomanana, A. Desopper :** *Weak coupling between an unsteady 3D Full Potential code and an unsteady turbulent boundary layer code. Application to a helicopter rotor in forward flight*, 30th AIAA Aerospace Sciences Meeting, Reno (Nevada), January, 1992

[9] **J. Cousteix :** *Theoretical analysis and prediction methods for a three-dimensional turbulent boundary layer.* ESA TT-238 Jan. 1976 (ONERA Publication N°157 (1974))

[10] **J. Cousteix :** *Three-dimensional boundary layers. Introduction to calculation methods.* In AGARD Report N°741 on Computation of three-dimensional boundary layers including separation. April 1986

[11] **J. Cousteix :** *Aérodynamique. Turbulence et couche limite.* Collection La Chevêche, CEPADUES-EDITIONS

[12] **P. Crozier :** *Recent improvements in rotor testing capabilities in the ONERA S1MA Wind Tunnel*, 20th European Rotorcraft Forum, Amsterdam (The Netherlands), October, 1994

[13] **A. Desopper :** *Etude expérimentale des couches limites turbulentes et transitionnelles en écoulement pulsé. Essais de prévision théorique.* Thèse de Docteur-Ingénieur ENSAE (Juin 1977)

[14] **P. S. Granville :** *The calculation of the viscous drag of bodies of revolution.* David Taylor Model Basin Report 849 (1953)

[15] **E. H. Hirschel, W Kordulla :** *Shear flow in surface-oriented coordinates.* Notes on numerical fluid mechanics, Vol 4, Vieweg, 1981.

[16] **R. Houdeville :** *Calcul de couches limites tridimensionnelles instationnaires par une méthode intégrale. Description de la méthode et mode d'emploi du code.* Rapport DERAT N°7/5031.09 juin 1995

[17] **M. Lazareff, J. C. Le Balleur :** *Computation of three-dimensional viscous flows on transonic wings by boundary layer-inviscid interaction*, La Recherche Aérospatiale, 1983-3 (1983) (english edition)

[18] **C. Polacsek, P. Lafon :** *High Speed Impulsive Noise and aerodynamic results for rectangular and swept blade tip in S1 Modane Wind Tunnel* , 17th European Rotorcraft Forum, Berlin (Germany), September, 1991

[19] **L. Rosenhead :** *Laminar Boundary Layers.* Fluid Motion Memoirs Oxford. Clarendon Press. 1963

[20] **Y. Semezis, P. Beaumier :** *Détermination de l'état de la couche limite sur des sections de pale d'hélicoptere à l'aide de films chauds*, 31^{ième} Colloque d'Aérodynamique Appliquée, Paris (France), 27-29 mars 1995

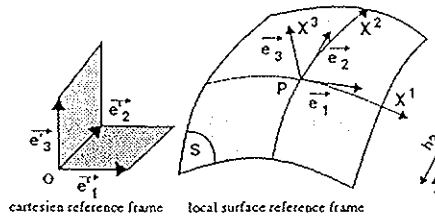

Figure 1: Body fitted coordinate surface and cartesian reference frame.

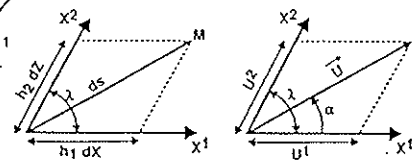

Figure 2: Metric elements and contravariant velocity components.

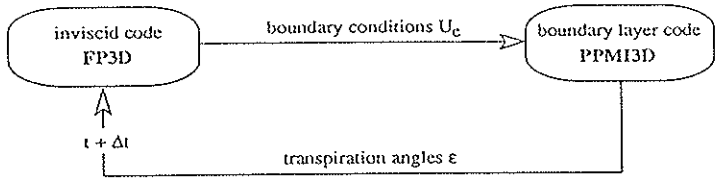

Figure 3: Coupling scheme between potential and boundary layer codes.

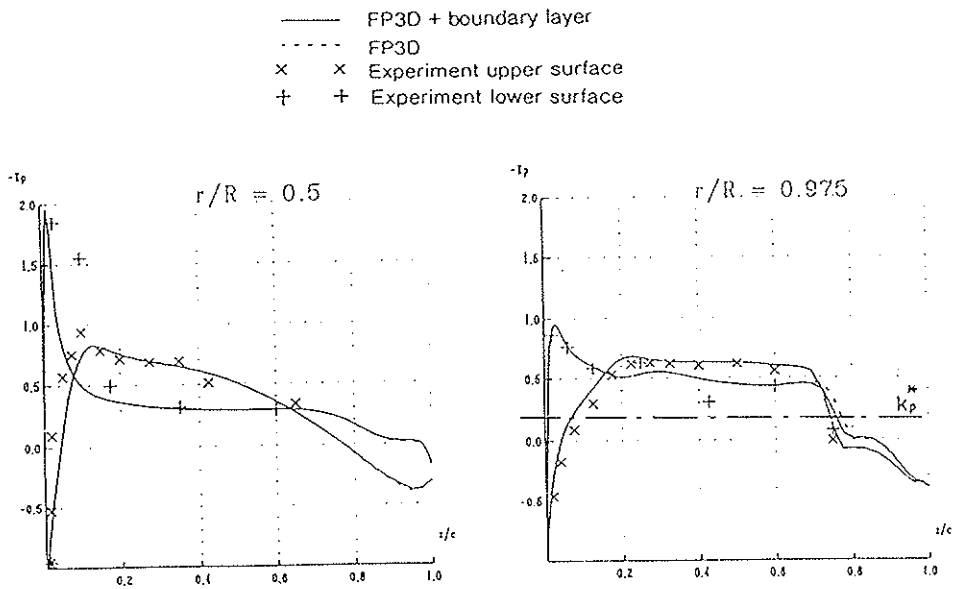

Figure 4: Pressure distributions (μ= 0.45).

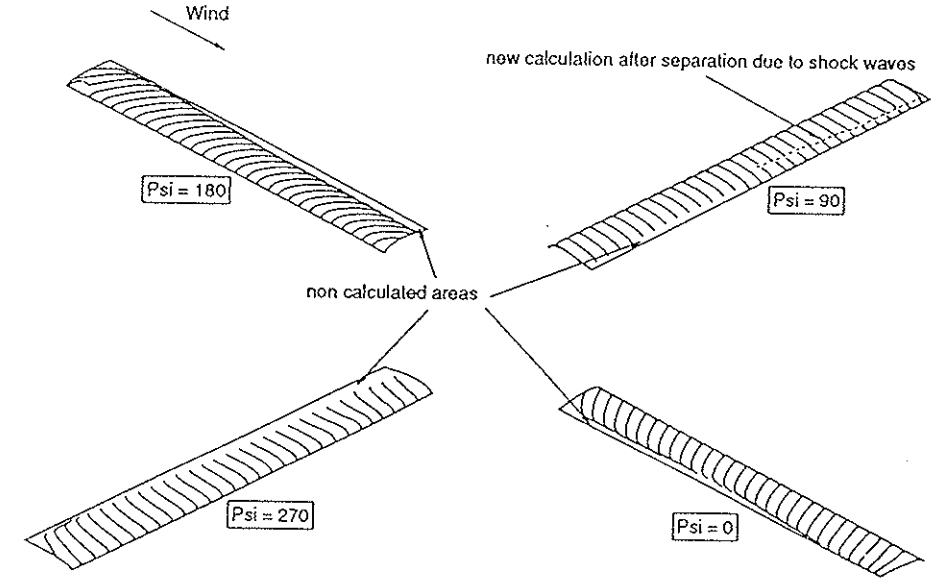

Figure 5: Skin friction lines on upper surface (μ= 0.45).

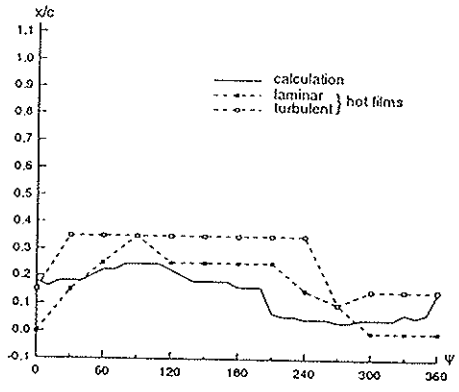

Figure 6: Laminar-turbulent transition (μ= 0.3, upper surface).

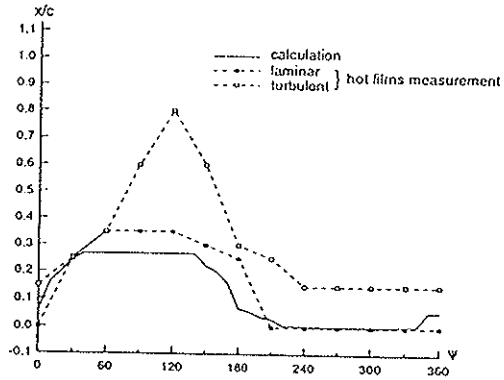

Figure 7: Laminar-turbulent transition (μ= 0.45, upper surface).

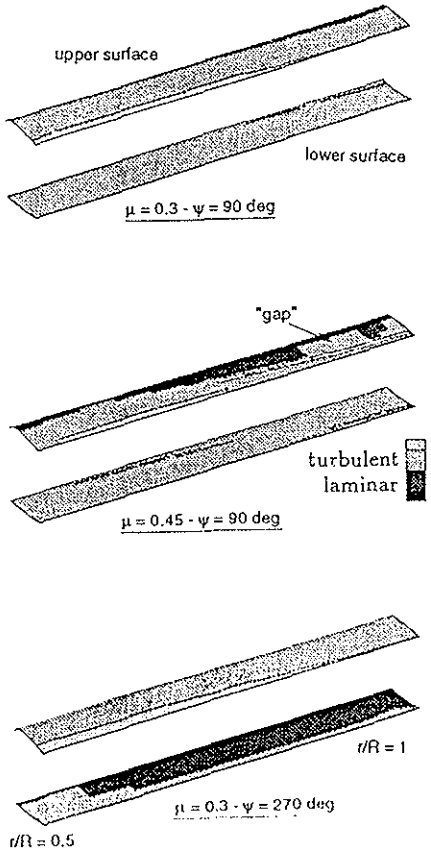

Figure 8: State of boundary layer (calculations).

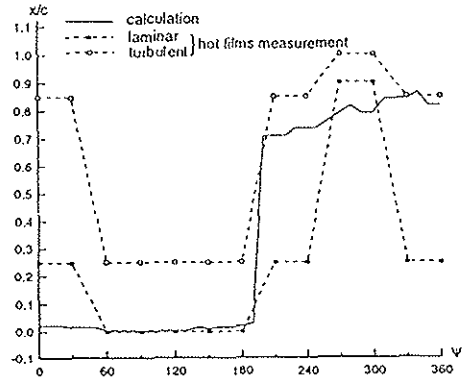

Figure 9: Laminar-turbulent transition (μ= 0.3, lower surface).

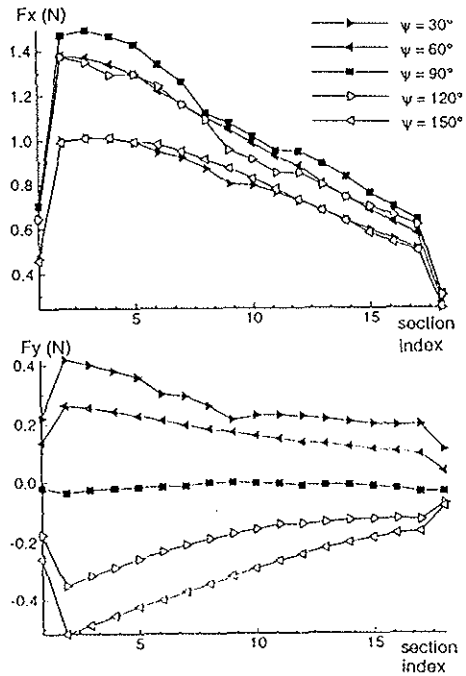

Figure 10: Friction forces on lower surface (μ= 0.45).

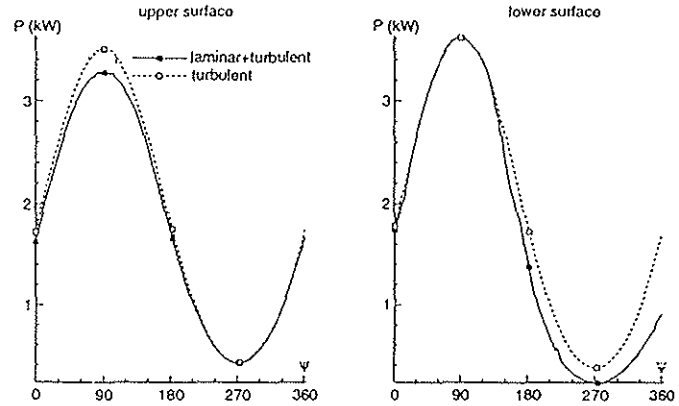

Figure 11: Effect of laminarity on viscous friction power (μ= 0.3).

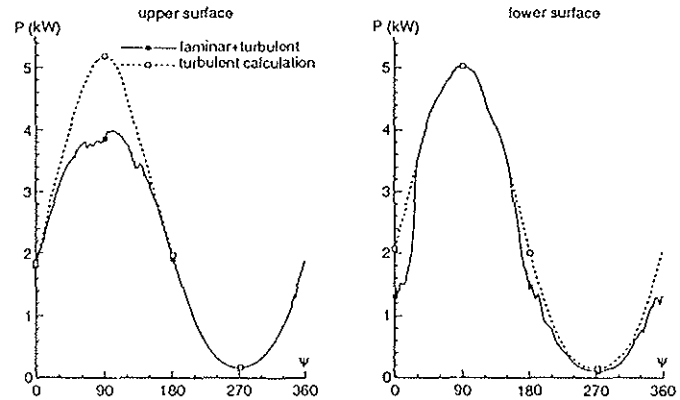

Figure 12: Effect of laminarity on viscous friction power (μ= 0.45).

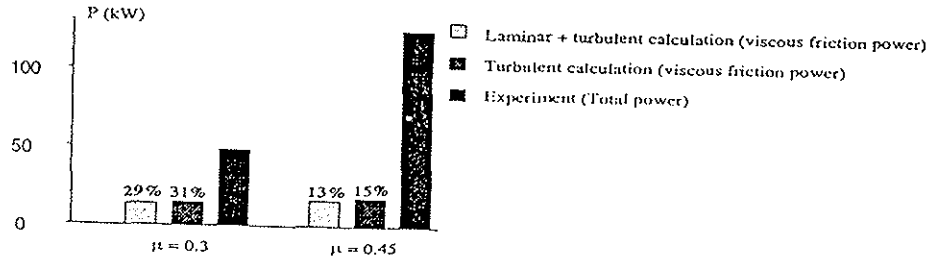

Figure 13: Effect of laminarity : comparison with total power.